



Zn-vacancy mediated electron-hole separation in ZnS/g-C₃N₄ heterojunction for efficient visible-light photocatalytic hydrogen production

Xuqiang Hao, Jun Zhou, Zhiwei Cui, Yicong Wang, Ying Wang*, Zhigang Zou*

School of Chemistry and Chemical Engineering, Eco-Materials and Renewable Energy Research Center (ERERC), National Laboratory of Solid State Microstructures, Kunshan Innovation Institute of Nanjing University, Nanjing University, Nanjing, 210023, PR China

ARTICLE INFO

Keywords:

Graphitic carbon nitride
Zinc vacancy
Heterojunction
Two-photo absorption
Photocatalytic hydrogen evolution

ABSTRACT

Vacancy defects play an important role in modifying the electronic structure and the properties of photoexcited charge carriers by introducing additional energy levels and consequently enhanced the photocatalytic activity of photocatalyst. In this work, we report a ZnS/g-C₃N₄ heterostructure with abundant zinc vacancy defects on the surface of ZnS to emphasize the synergistic promotion on charge separation. The ZnS/g-C₃N₄ heterostructured photocatalyst possesses low over-potential, extended absorption in the visible light region, and promoted photoinduced electron-hole separation capability. Fluorescence emission spectra and XPS results confirm that existence of abundant zinc vacancies on ZnS. V_{Zn}-rich CZV20 (g-C₃N₄/ZnS-20 wt%) heterojunction exhibits more than 30 times higher photocatalytic H₂ evolution rate (713.68 μmol h⁻¹ g⁻¹) than that of pure g-C₃N₄ (24.09 μmol h⁻¹ g⁻¹) under visible light irradiation and high stability during the prolonged photocatalytic operation. The enhanced photocatalytic performance can be attributed to the intimate interfacial contact between g-C₃N₄ and ZnS nanoparticles, increasing the light-absorbing capacity and charge separation efficiency of ZnS/g-C₃N₄ heterojunction. And more importantly, the visible-light photocatalytic H₂ production activity can be ascribed to the two-photo excitation in the middle band gap of ZnS. This work demonstrates that appropriate Zn vacancy defects modified ZnS/g-C₃N₄ heterojunction can be used for highly efficient visible-light photocatalysis.

1. Introduction

Solar-driven photocatalysis for hydrogen evolution from water splitting has emerged as one of the most attractive renewable energy technology to address the energy crisis and environmental issues [1,2]. However, it is still a great challenge to find/explore an ideal photocatalyst for practical use with relatively high active, low-cost, and long-term stable under visible light. To date, numerous efforts have been taken to develop suitable semiconductor photocatalysts to obtained high activities for water splitting [1–6]. However, much major limitations to achieve high photocatalytic efficiency utilizing solar energy are restricted by the light absorption and the fast recombination of electron-hole pairs [6]. Thus, the improvement of charge separation and light absorption have been proven to be crucial to enhance the photocatalytic performance [7]. For instance, contracting heterostructured photocatalysts which depends on the band offsets of the two semiconductors have been demonstrated as an effective way to promote the spatial charge separation and photocatalytic property [7,8].

Recently, graphitic carbon nitride (g-C₃N₄) as metal-free conjugated polymeric semiconductor is identified as one of the most promising

photocatalytic materials and has been receiving enormous research attention in photocatalysis due to its visible-light response with suitable band gap (2.7 eV), nontoxicity, excellent chemical stability, and low cost convenient preparation methods, and so forth [9–19]. However, its drawbacks such as low optical absorption in the visible-light region, small surface areas (~10 m²/g) and ultrafast photogenerated electron-hole recombination rate, which severely restrict the photocatalytic activity of pristine bulk g-C₃N₄ [20,21]. Thus, it is most important to rationally design and synthesize g-C₃N₄-based photocatalysts to enhance the visible-light absorption ability and accelerate the separation of photogenerated charge carriers. Various strategies have been investigated to modify g-C₃N₄, such as nanostructure engineering [22–24], defect engineering [25–29], co-polymerization [30,31], non-metal elements doping (C, P, S, Br) [32–34], loading with precious metal (Ag, Pt) [35,36], constructing heterojunction [37–50] or all solid-state Z-scheme systems [40]. Especially, heterostructure contraction of g-C₃N₄ has been considered as an effective strategy to greatly enhanced charge carrier separation efficiency and photocatalytic performance [37]. So far, various kinds of g-C₃N₄-based heterostructure photocatalysts, for example, CdS/g-C₃N₄ [39], TiO₂/C₃N₄ [40–42], NiS/g-

* Corresponding authors.

E-mail addresses: wangy@nju.edu.cn (Y. Wang), zgrou@nju.edu.cn (Z. Zou).

C₃N₄ [43], black phosphorus/g-C₃N₄ [44], carbon/g-C₃N₄ [45] and NH₂-MIL-125(Ti)/g-C₃N₄ [46] have been reported with the considerable photocatalytic activity. Zinc sulfide is a superior photocatalyst for H₂ evolution, whereas the wide bandgap restricts its performance to only UV region. Although there are few reports on the ZnS microsphere/g-C₃N₄ nanocomposite and ZnS/g-C₃N₄ heterojunction with enhanced performance for hydrogen evolution [47,48], however, to the best of our knowledge, there is no report on the defect engineering on ZnS/g-C₃N₄ heterojunction photocatalysts to enhance visible-light-harvesting ability and charge separation for improving photocatalytic hydrogen production activity.

As is well known, defect engineering on the photocatalysts is an appealing strategy for enhancing light harvesting and carrier separation efficiency in photocatalytic materials [51,52]. Defects in semiconductor photocatalysts not only can introduce new energy levels to narrow the band gap that regulate the light absorption behavior, but also dominate the kinetics of charge transfer for effective charge separation and prevent the recombination of photogenerated charge carriers. It is worth noting that controlling the amount of defects is great important to photocatalytic reaction, because excessive amount defects can act as recombination centers for charge carriers and hence decreasing the photocatalytic activity. Vacancy-rich materials with good electron transfer property are of great interest [53]. Vacancy defects can play an important role in modifying the electronic structure and the properties of photoexcited charge carriers by introducing additional energy levels and consequently enhanced the photocatalytic activity of photocatalyst [24–28]. Many researchers have reported that the vacancy defects on the surface of catalysts may induce positive effects on photocatalytic reactions. For example, oxygen vacancies are one of kind of intrinsic defects in crystals, which have been found to play a crucial role in TiO₂ [54], ZnO [55,56], Fe₂O₃ [57], BiOCl [58,59], BiO_{2-x} [60] photocatalysts for improving visible-light response. Furthermore, the nitrogen vacancies and carbon vacancies also can significantly redshift the absorption edge of g-C₃N₄ with superior visible-light photocatalytic performance compared to pristine g-C₃N₄ [24–28]. Recently, it is reported that S vacancies in ZnS can induce an excellent photocatalytic activity for H₂ production under visible light [61,62]. And the photocatalytic activity of ZnS increases steadily with increasing the concentration of S vacancies, which can serve as photosensitization units that induce visible light response and as active sites that trap electrons for proton reduction [61,62]. Moreover, the Zn vacancies (V_{Zn}) are also beneficial to modify the light absorption behavior and narrow the bandgap of ZnS film for photocatalysis under visible-light irradiation. It was reported that the Zn-deficient ZnS film with a band gap of ~2.4 eV was fabricated by pulsed laser deposition (PLD) with controlling the N₂ background pressure. It exhibits a high photocurrent density of 1.5 mA cm⁻² under visible light irradiation ($\lambda \geq 435$ nm) [63]. Most recently, ZnS nanoparticles with Zn vacancy and interstitial sulfur states were prepared using ultrasonic methods, which exhibited more outstanding photocorrosion stability and photocatalytic activity for degrading reactive black 5 (RB5) under visible light irradiation [64]. In particular, it is also demonstrated in our recent work, changing the molar ratio of zinc acetate and sodium sulfide in one-pot hydrothermal process can produce different amount of zinc vacancies on the surface of ZnS, greatly adjusting its band structure and hence tuning the electronic band structure [65]. These results clearly confirm Zn vacancies engineering is a potential approach for regulate the light absorption behavior and photostability in photocatalysis.

In this work, we reported an integrated design and synthesis of ZnS/g-C₃N₄ heterostructure with abundant zinc vacancy defects on the surface of ZnS to emphasis the synergistic promotion on charge separation. The constructing ZnS/g-C₃N₄ heterostructured photocatalyst is facilitated to spatial charge separation for improving photocatalytic hydrogen production, and it possess low over-potential, extended absorption in the visible light region, and promoted photoinduced electron – hole separation capability. The enhanced photocatalytic

performance can be attributed to the intimate interfacial contact between g-C₃N₄ and ZnS nanoparticles, accelerating the charge transfer, as well as zinc vacancy defects, increasing the light-absorbing capacity and accelerating the charge transfer of ZnS/g-C₃N₄ heterojunction. This work highlights the vacancy defects modification of ZnS/g-C₃N₄ heterojunction maybe a feasible strategy for improving charge separation and photocatalytic performance.

2. Experimental section

2.1. Preparation of photocatalysts

2.1.1. Preparation of the g-C₃N₄

Bulk g-C₃N₄ was prepared by directly heating melamine in a tubular furnace. In a typical procedure, 5 g melamine was heated at 550 °C for 4 h at a heating rate of 7 °C min⁻¹ in a closed system with a cover at air atmosphere. After cooling to room temperature, the resultant yellow product was collected and milled into a powder for further use.

2.1.2. Synthesis of the zinc-vacancy ZnS/g-C₃N₄ heterojunction photocatalysts

ZnS/g-C₃N₄ heterostructure photocatalysts with different weight ZnS were prepared by a one-pot hydrothermal method using Zn (Ac)₂·2H₂O, Na₂S·9H₂O and g-C₃N₄ as the starting materials. Typically, 1 g bulk g-C₃N₄ was first dispersed into 20 mL deionized water via ultrasound treatment at room temperature for 1 h. Then, the pre-determined Zn(Ac)₂·2H₂O and Na₂S·9H₂O (molar ratio = 1:2.5) was dissolved in the g-C₃N₄ dispersed solution under constant magnetic stirring. After stirring for 60 min, the yellow white mixture solution was then transferred into a 50 mL Teflon-lined autoclave and maintained at 160 °C for 12 h. Finally, the light yellow precipitate was obtained by centrifugation and washed several times with deionized water and ethanol and vacuum dried at 60 °C overnight. The as-prepared zinc-vacancy ZnS/g-C₃N₄ samples are denoted as g-C₃N₄/ZnS-X% (namely, CZVX), where “X” is 10, 15, 20, 25, 30, which stands for the weight content of ZnS. As a reference, pure zinc-deficient ZnS was also prepared as control using the same method without g-C₃N₄.

2.2. Characterizations

Powder X-ray diffraction (PXRD) data were collected using a Rigaku Ultima III X-ray diffractometer using Cu K α radiation ($\lambda = 1.54056$ Å). Fourier transformed infrared (FTIR) spectra were performed on a Nicolet NEXUS870 spectrometer using the KBr pellet support. Scanning electron microscope (SEM) images were recorded with a Hitachi S4800 FE-SEM system. Transmission electron microscope (TEM) and high-resolution transmission electron microscope (HRTEM) images were obtained by using a JEM-2100 electron microscope. X-ray photoelectron spectroscopy (XPS) measurements were performed using PHI 5000 Versa Probe X-ray photoelectron spectrometer (a monochromatic Al K α X-ray radiation). All of the binding energies of all elements were calibrated by the C 1s peak at 284.6 eV. UV – vis spectra were collected using a Shimadzu UV-3600 spectrometer, BaSO₄ was used as reference. The photoluminescence (PL) spectra were taken on a Horiba Scientific FluoroMax-4 fluorometer spectrometer at room temperature and Time-resolved fluorescence emission spectrum were conducted with Horiba Jobin Yvon Data Station by time-correlated single-photon counting. Unconverted PL were examined on a FLS 980 fluorometer spectrometer. Electron paramagnetic resonance (EPR) spectra were recorded on a Bruker EMX-10/12 EPR spectrometer at room temperature.

2.3. Photocatalytic hydrogen evolution

The photocatalytic hydrogen evolution reactions were conducted in a side-irradiation Pyrex reactor, which connected to a glass-closed gas circulation system at ambient temperature. In a typical photocatalytic

experiment, 50 mg of catalyst power was suspended in 400 mL aqueous solution containing Na_2S and Na_2SO_3 as the sacrificial agent of the hole. Before visible light irradiation, the reactant system was degassed by evacuation to remove air and ensure that the reaction system was under anaerobic conditions, and then was irradiated by a 300-W Xe lamp with a cutoff filter of 420 nm for H_2 evolution under magnetic stirring condition. The amount of hydrogen evolution was analyzed by an online gas chromatograph (GC-14C, Shimadzu, TCD, Ar as carrier).

2.4. Electrochemical measurements

The photoelectrochemical measurement was performed on an electrochemical analyzer (Chenhua CHI 660D) in a standard three-electrode cell. The working electrodes were prepared as follows: 10 mg of photocatalyst powder and 20 μL 0.25% Nafion were dispersed into 1.0 mL ethanol, and then milled into slurry in a small agate mortar. The slurry about 50 μL was then directly coated onto the precleaned indium tin oxide glass (ITO glass) surface ($1 \times 2 \text{ cm}^2$). Finally, the obtained electrodes were heated to 120°C for 1 h in the oven. Platinum wire was used as the counter electrode, and a saturated calomel electrode (SCE) was used as the reference electrode. $E^\circ = 0.241 \text{ V}$ vs. NHE at 25°C for saturated calomel electrode. The Mott-Schottky curves were taken under dark with a voltage of 5 mV at a frequency of 2.0, 1.5 and 1.0 kHz. The potential ranged from -1.5 to 1.0 V (vs. SCE). Electrochemical impedance spectroscopy (EIS) plots were collected at open circuit potential (0.5 V vs. SCE), with the frequency ranging from 100 kHz to 0.01 Hz and the modulation amplitude of 5 mV. The transient photocurrent measurements were recorded at an applied potential of 0.5 V vs. SCE under the visible light illumination. A 300-W Xe lamp equipped with an optical cutoff filter of 420 nm was employed for the visible-light excitation. The electrocatalytic activity of the samples were examined by obtaining polarization curves using linear sweep voltammetry (LSV) with a scan rate of 5 mV s^{-1} at room temperature.

3. Results and discuss

3.1. Structure and morphology analysis

The phase structures of the $\text{g-C}_3\text{N}_4$, ZnS and ZnS/ $\text{g-C}_3\text{N}_4$ photocatalysts are determined by the powder X-ray diffraction (XRD), as shown in Fig. 1a. It can be clearly observed that pure $\text{g-C}_3\text{N}_4$ displayed two characteristic diffraction peaks at 13.20° and 27.75° , which corresponding to the (100) and (002) planes of polymeric $\text{g-C}_3\text{N}_4$ (JCPDS #87-1526) [50]. The peak at 13.20° was assigned to the hydrogen bonds maintaining interlayer long-range atomic order between tri-s-triazine units with an interplanar distance of 0.675 nm [66]. The peak centered at 27.75° was related to the graphitic layer stacking which

controlled by the Van der Waals force, which give an interplanar distance $d = 0.321 \text{ nm}$ [66]. For the pure ZnS, four main characteristic peaks centered at 28.73° , 33.29° , 47.75° and 56.53° can be observed, which belong to the (111), (200), (222) and (311) planes, respectively, that can be well indexed to cubic sphalerite ZnS (JCPDS#05-0566) [47]. For the ZnS/ $\text{g-C}_3\text{N}_4$ composites, all the characteristic peaks fit well with both cubic ZnS and $\text{g-C}_3\text{N}_4$, and there are no other impure peaks can be observed, indicating these composites consist of two phases. Impressively, the relative intensity of $\text{g-C}_3\text{N}_4$ (002) peak at 27.75° decreases with increasing ZnS loading, while the intensities of ZnS increase with the increasing amount of ZnS. According to the Debye-Scherrer formula ($D = K\lambda/(\beta\cos\theta)$), the particle size of ZnS is about 16.44, 11.01, 13.88, 14.66, 15.93, 19.34 nm for of pure ZnS, CZV10, CZV15, CZV20, CZV25 and CZV30 on the basis of (220) peak, respectively. Notably, based on the enlarged view in Fig. 1, the (111) plane of ZnS/ $\text{g-C}_3\text{N}_4$ samples has a slight shift toward higher angles from 28.73° to 28.83° , suggesting a progressively smaller lattice spacing of (111) plane for the sphalerite ZnS ($d = 0.301 \text{ nm}$) in comparison of pure ZnS ($d = 0.311 \text{ nm}$). In addition, the (002) peak of ZnS/ $\text{g-C}_3\text{N}_4$ samples also shifts toward higher angles from 27.75° to 27.96° compared with that of bulk $\text{g-C}_3\text{N}_4$, implying a narrowing interlayer distance ($d = 0.319 \text{ nm}$) between the layers of $\text{g-C}_3\text{N}_4$ [28,43]. It may be the increased nitrogen defects resulted in an increased electron density which strengthen the π - π interaction between interlayers lead to a narrowing interlayer distance. The increased nitrogen defects have been testified by XPS and EPR and shown later. In contrast, the (100) peak of ZnS/ $\text{g-C}_3\text{N}_4$ samples almost disappears compared with the bulk $\text{g-C}_3\text{N}_4$, demonstrating the decrease amount of hydrogen bonds after hydrothermal treatment in Na_2S alkaline aqueous solution. It has been reported that the smallest amount of hydrogen bonds is facilitate to the charge transfer between inter-layers of carbon nitride, which resulting in superior photoactivity [66]. However, the contribution of hydrogen bond for improving photocatalytic activity is similar to the all of ZnS/ $\text{g-C}_3\text{N}_4$ samples from the (100) peak intensity of $\text{g-C}_3\text{N}_4$.

To further confirm the molecular structure of the CZV20 heterojunction, FT-IR spectroscopy is performed. As shown in the spectra of all ZnS/ $\text{g-C}_3\text{N}_4$ heterojunctions (Fig. 2a), the distinctive stretch modes do not have any obvious change with $\text{g-C}_3\text{N}_4$ which directly certify the molecular structure integrity of $\text{g-C}_3\text{N}_4$. In Fig. 2a, the broad peak of CZV20 near 3185 cm^{-1} is related to N–H stretching vibration modes in $\text{g-C}_3\text{N}_4$, while the absorption peaks at 1200 – 1650 cm^{-1} are assigned to typical molecular framework containing $\text{sp}^2 \text{ C} = \text{N}$ or $\text{sp}^3 \text{ C} - \text{N}$ heterocycles stretching vibrations [40,43]. The prominent peaks at 1239 , 1315 and 1404 cm^{-1} can be ascribed to the characteristic stretching vibration modes of C–NH–C units of $\text{g-C}_3\text{N}_4$, while the absorption peaks at 1574 and 1643 cm^{-1} are assigned to C = N stretching vibration modes [47]. The characteristic absorption peak centered at

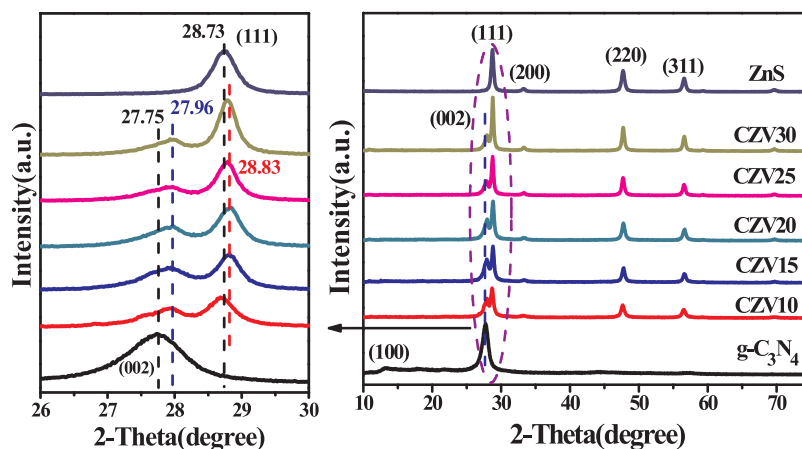


Fig. 1. XRD patterns of as-prepared $\text{g-C}_3\text{N}_4$, ZnS and ZnS/ $\text{g-C}_3\text{N}_4$ samples.

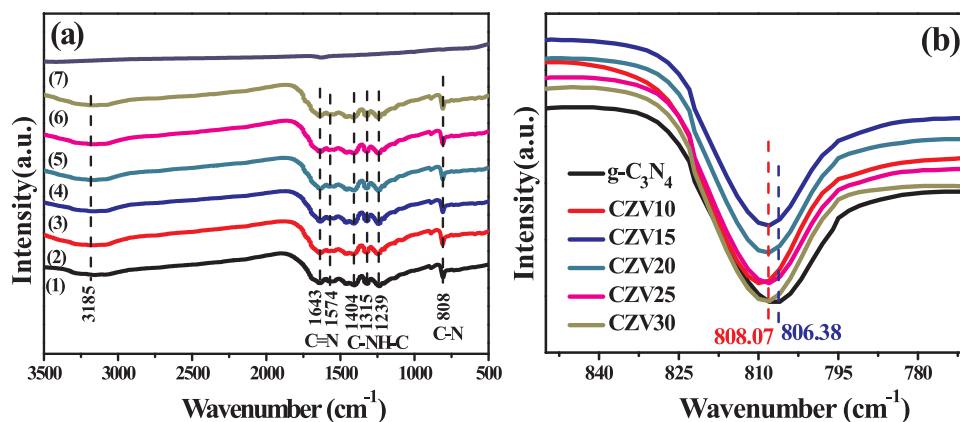


Fig. 2. FT-IR spectra of (a) pure g-C₃N₄ (1), CZV10 (2), CZV15 (3), CZV20 (4), CZV25 (5), CZV30 (6) and ZnS (7); (b) the enlarged view of a.

approximately 808 cm⁻¹ is attributed to aromatic C–N stretching of tri-s-triazine units [50]. Moreover, the absorption peak of tri-s-triazine units for ZnS/g-C₃N₄ samples is blue-shifted to 806 cm⁻¹ from 808 cm⁻¹ in the enlarged view of Fig. 2b, indicating a decreased electron cloud density in tri-s-triazine units which probably caused by the N-coordinated Zn atoms. For the tertiary nitrogen groups, the lone pair electrons of sp³-hybridized N atoms as electron donors can interact with the unoccupied d orbitals of Zn atoms to form a N–Zn bond. Such chemical coupling will lead to a decreased electron density in N along with increased electron density in Zn to form covalent Zn–N bonding states. The decrease of electron cloud density further testified the lower amount of hydrogen bonds in ZnS/g-C₃N₄ samples, which agrees well with the XRD results about (100) plane.

The morphology of as-synthesized g-C₃N₄ and CZV20 samples is investigated by SEM and TEM. As depicted in Fig. 3a, the pure g-C₃N₄ exhibit a lamellar stacking structure with folded edges. In Fig. 3b, the ZnS nanoparticles highly dispersed on the surface of layered g-C₃N₄. Such spatial distribution of ZnS nanoparticles on g-C₃N₄ affords more active sites for photocatalytic hydrogen evolution.

The transmission electron microscopy (TEM) image of the g-C₃N₄ (Fig. 4a) further indicates it a lamellar stacking structure. The TEM image of the CZV20 sample from Fig. 4b revealed that ZnS is a spherical-like nanoparticle with mean size of around 30.65 nm (Fig. S1), which is tightly grown on the surface of g-C₃N₄ nanosheets. From the high-resolution TEM (HRTEM) image in Fig. 4c, the lattice fringes of ZnS can be clearly observed, and the spacing values of lattice fringes is 0.297 nm corresponding to the (111) plane of the sphalerite ZnS, which is well agreement with the XRD results. In addition, the SAED pattern of CZV20 inserted in Fig. 4c confirms that the in situ grown ZnS nanoparticles on g-C₃N₄ have an excellent crystallinity. Intriguingly, both the distinct and blurry lattice fringes are observed in the white square frame region of Fig. 4c, and the enlarged white square frame region are

shown in Fig. 4d. The observed blurry lattice fringes in red circle region (Fig. 4d) imply there is abundance of zinc vacancies exist in the surface of ZnS, which have been demonstrated in our previous work and will be further verified by XPS and PL techniques [65]. The thickness of surface zinc vacancies layer is 1–5 nm. These surface zinc vacancies derive from the excess of Na₂S with Zn²⁺ disturbs the surface lattice of ZnS in the hydrothermal reaction process, which results in zinc deficient-ZnS [65]. This surface zinc vacancies serve as trap sites that are beneficial to prevent the recombination of the photoinduced charges and enhance the electron transfer for photocatalytic H₂ production.

To confirm the surface chemical states of CZV20 heterojunction sample, the X-ray photoelectron spectroscopy (XPS) was carried out. The C 1s at 284.6 eV was used as a reference to correct the binding energies. The survey spectrum of g-C₃N₄, ZnS and CZV20 samples are shown in Fig. S2. In comparison with g-C₃N₄ and ZnS, CZV20 is mainly consist of C, N, Zn, S and O elements, which verify the successful immobilizing of ZnS on the g-C₃N₄ nanosheets. As depicted in Fig. 5a, the C1s XPS spectra for g-C₃N₄ can be divided into three peaks at 284.6, 286.1 and 287.9 eV. The peak at 284.6 eV is assigned to the reference carbon and graphitic carbon. The peaks at 286.1 and 287.9 eV are ascribed to the C–NH₂ species on the edges of heptazine units and sp²-bonded carbon N–C=N aromatic rings in the framework of g-C₃N₄, respectively [28]. The N 1s XPS spectrum (Fig. 5b) for g-C₃N₄ contained three components at 398.8, 399.9 and 401.1 eV, corresponding to the bicoordinated sp²-hybridized nitrogen C–N=C of triazine rings, tertiary nitrogen groups N₃C nitrogen atoms and nitrogen bonded with hydrogen atoms N–H_x functional groups, respectively [40]. In Fig. 5c, the Zn 2p XPS spectra for pure ZnS shows two peaks at 1021.4 eV and 1044.4 eV, which are assigned to Zn 2p_{3/2} and Zn 2p_{1/2} respectively [65]. The S 2p XPS spectrum of ZnS (Fig. 5d) is fitted by four peaks at the binding energies of 160.4, 160.8, 161.3 and 162.4 eV. The peaks at 160.4 and 161.3 eV are attributed to the S 2p_{3/2} and S 2p_{1/2} for the

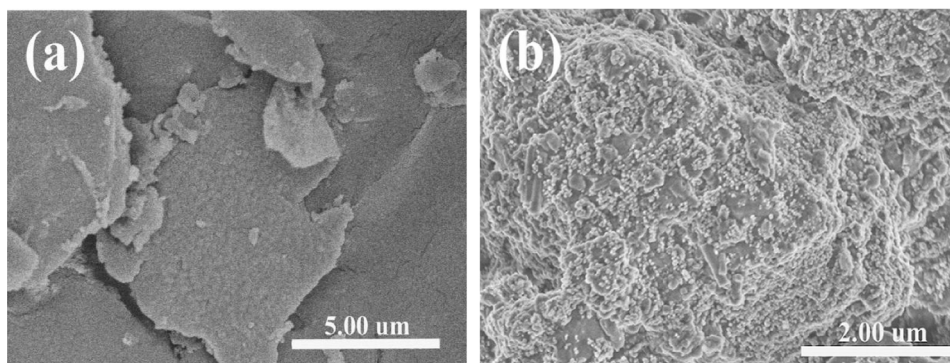


Fig. 3. SEM images of (a) pure g-C₃N₄ and (b) CZV20 sample.

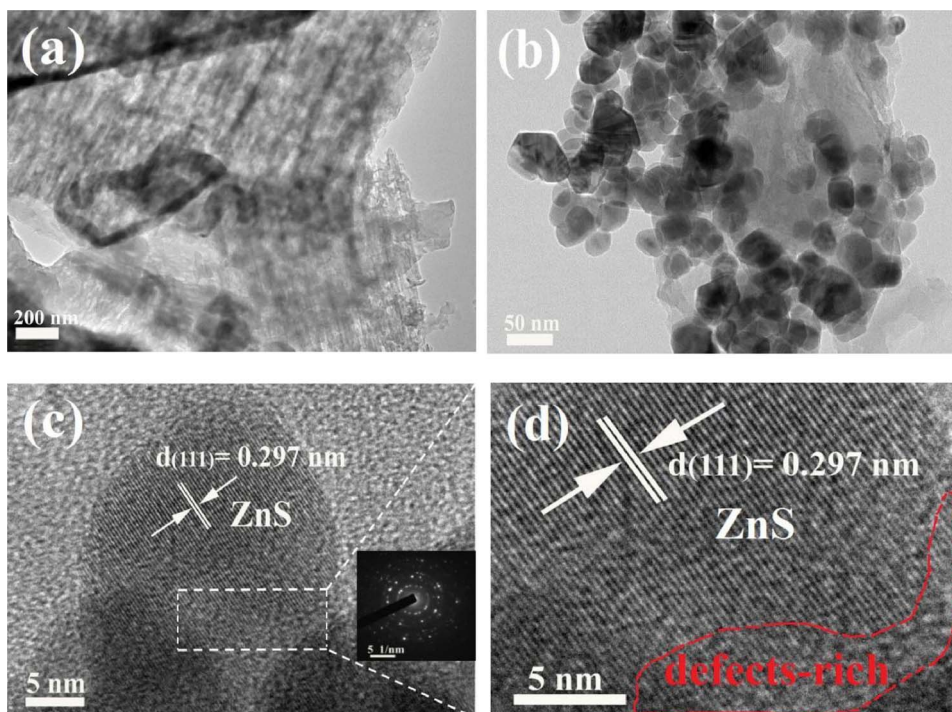


Fig. 4. TEM images of (a) g-C₃N₄ and (b) CZV20 samples; (c) HRTEM images of CZV20, the insert is corresponding SAED pattern; (d) the enlarged view of c.

basal sulfide ion (S^{2-}), whereas the S 2p peaks at 160.8 and 162.4 eV assigned to the bridging S_2^{2-} and apical S^{2-} in the ZnS [67], indicating that the existence of a number of unsaturated edge S atoms on the surface of ZnS. And this result further indicating that the existence of

the vacancy defect states in the ZnS structure. Moreover and interestingly, for the CZV20 nanocomposite, it can be clearly observed that the binding energies of C 1s, N 1s, Zn 2p and S 2p have systematically shifted towards low binding energies with 0.2–0.8 eV compared to

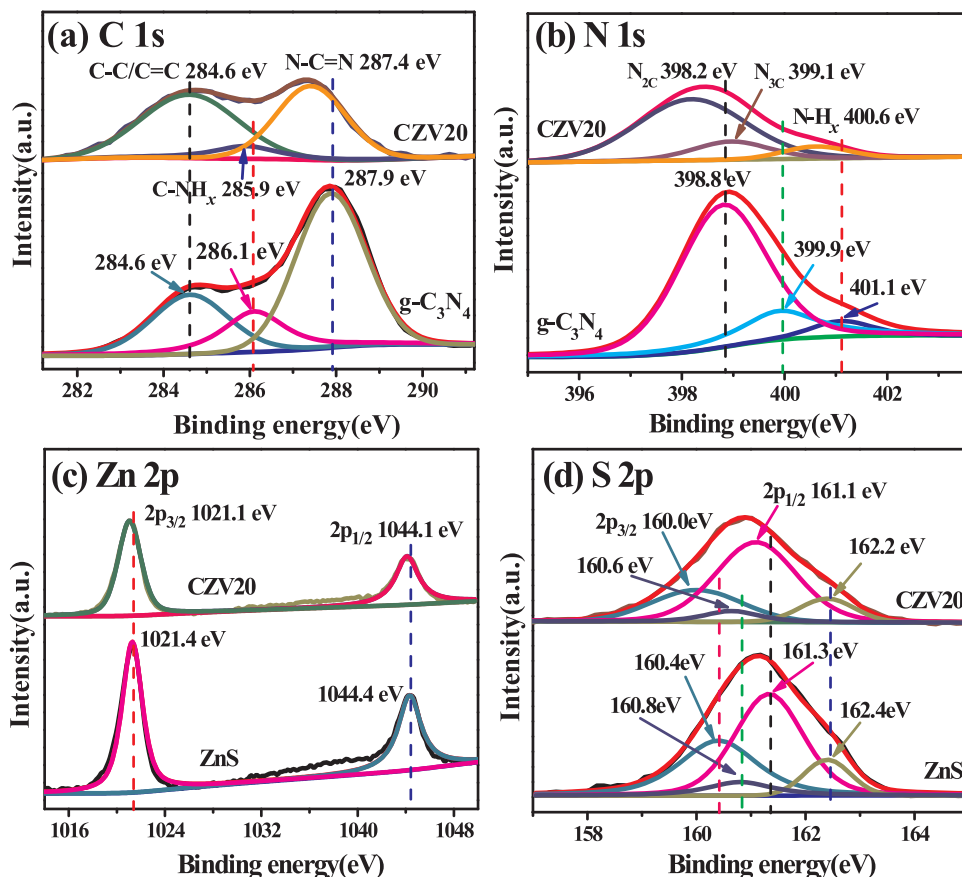


Fig. 5. XPS spectra of (a) C 1s, (b) N 1s, (c) Zn 2p and (d) S 2p for the g-C₃N₄, ZnS and CZV20.

Table 1
The chemical composition of ZnS and CZV20 measured by XPS.

Samples	Zn (at.%)	S (at.%)	Zn:S
ZnS	0.46	0.54	0.85:1
CZV20	0.44	0.56	0.78:1

pristine g-C₃N₄ and ZnS, which is attributed to change of surface electron density. It has been reported that the variation of binding energies relates to the change of surface electron density, which results from electron transfer between semiconductors with different Fermi energy (E_F) [68]. The electron will transfer from high E_F to lower E_F . Thus, electrons will transfer from g-C₃N₄ to ZnS in the ZnS/g-C₃N₄ hybridization process, resulting in a decrease of electron concentration in g-C₃N₄ and an increase in ZnS, thus, the binding energies of Zn 2p and S 2p decreased [68]. The surface zinc vacancies also increase the surface electron density [53]. The binding energies of C 1s and N 1s shifted towards low binding energies may be ascribed to the nitrogen vacancies which lead to a much higher concentration of delocalized electrons, and it will be verified by EPR afterwards. Most importantly, the quantitative XPS elemental analysis (Table 1) confirmed that the Zn vacancy exist in surface region of ZnS and CZV20 [65]. The Zn:S atomic ratio of ZnS and CZV20 are 0.85:1 and 0.78:1, respectively, both are lower than ZnS stoichiometry Zn:S atomic ratio of 1:1. As demonstrated in our previous work, the atomic ratio $Zn/S < 1$ is an important sign for the existence of Zn vacancy [65]. And the amount of Zn vacancy is increasing with the concentration of Na₂S increased, that is, the amount of Zn vacancy is increasing with the loading ZnS increased [65].

3.1.1. Optical and electronic properties

The photoluminescence (PL) of pure g-C₃N₄ and ZnS/g-C₃N₄ solid powder samples were carried out to investigate the migration, separation efficiency and recombination processes of photogenerated electron-hole pairs at room temperature. Fig. 6a shows the PL spectra of pure g-C₃N₄, CZV10, CZV15, CZV20, CZV25 and CZV30 with an excitation wavelength of 340 nm, respectively. The PL spectra of pure g-C₃N₄ has a strong emission peak centered at 458 nm, which can be ascribed to the radiative recombination process of self-trapped excitations [69]. Obviously, after coupling with ZnS, the PL emission intensity significantly decreased, demonstrating the efficient charge separation and slower photogenerated electron-hole recombination rate in ZnS/g-C₃N₄ heterojunctions compared with pure g-C₃N₄. It can be demonstrate that there are strong interactions between ZnS and g-C₃N₄ and the formation of interface structure between the ZnS and g-C₃N₄ is beneficial to the interfacial charge transfer. Notably, the CZV20 heterojunction showed the weakest PL intensity among the all as-prepared composites, which could be attributed to the effective interfacial charge

transfer between ZnS and g-C₃N₄. This efficient electron transfer process of ZnS/g-C₃N₄ will not only benefit the electron-hole separation but also promote the increase of the photocatalytic efficiency. The PL is an effective method for detecting point defects of ZnS, such as S vacancy and Zn vacancy [70–73]. In Fig. 6b, there are four peaks appeared for pure ZnS, the emission peak at 369 nm can be attributed to the near band edge emission, while other three peaks at 436, 468 and 525 nm can be ascribed to zinc vacancy defect-states emission [70–72]. Of note, the formation of zinc vacancies resulted in the dangling S bonds, which could accommodate electrons [53]. These surface defects influence the luminescence properties of catalysts and causes nonlinear optics effects, for instance, two-photo absorption or multi-photo absorption [74–76]. And the two-photo absorption of zinc vacancy typed ZnS was further confirmed by the upconverted PL (Fig. S3) under the excitation of 532nm and 633 nm. In addition, six fitting peaks at 436, 451, 468, 488, 501 and 525 nm are observed in the Fig. S4, the emission peak at 451 nm can be attributed to the g-C₃N₄, while the peaks at 436, 468, 488, 501 and 525 nm can be ascribed to the zinc vacancies defect-states of ZnS [64,70–72]. And there is not observed S vacancy defects in our prepared samples according to the PL results. Thus, the PL emission intensity of CZV20 drastically decreased could be attributed to the synergistic charge transfer effect of heterostructure and zinc vacancies.

To further gain more insight into the promoting effect of zinc vacancy ZnS for charge separation and transfer in the obtained g-C₃N₄/ZnS system, the time-resolved fluorescence (TRPL) decay spectra are performed on pure g-C₃N₄ and CZV10, CZV20, as shown in Fig. S5. All the double-exponential fitting results are summarized in Table S1. The average lifetime $\langle \tau_{av} \rangle$ for g-C₃N₄ is 7.15 ns, while for the CZV10 and CZV20 are 5.90 ns and 4.13 ns, respectively. Both of two fluorescence lifetimes of g-C₃N₄/ZnS composites are shortened. This result further illustrated that the defect energy states of zinc vacancy ZnS provided extra nonradiative pathways for charge carrier transfer, which was accountable for the shortening fluorescence lifetime as well as the quenching of steady-state PL emission [77]. The rates of the non-radiative transfer $\langle k_{ent} \rangle$ listed in Table 1 were calculated according to the equation $\langle k_{ent} \rangle = \langle \tau_1 \rangle^{-1} - \langle \tau_2 \rangle^{-1}$, and the τ_1 and τ_2 are the short and long lifetimes, respectively [78]. The rate of the energy transfer of CZV20 was 1.07 times as high as that of g-C₃N₄. Moreover, the electron-transfer rate $\langle k_{et} \rangle$ was calculated to be 0.030 ns⁻¹ and 0.102 ns⁻¹ corresponding to CZV10 and CZV20 by the equation $\langle k_{et} \rangle = \langle \tau(CZV20) \rangle^{-1} - \langle \tau(g-C_3N_4) \rangle^{-1}$, respectively, where $\tau(CZV20)$ and $\tau(g-C_3N_4)$ are the average PL lifetimes for the CZV20 and g-C₃N₄, respectively [78,79]. The electron-transfer rate $\langle k_{et} \rangle$ is 3.4 times as high as that of CZV10. This results further demonstrated that important role of the zinc vacancy ZnS in promoting energy transfer and electron-transfer rates [78].

UV-vis diffuse reflectance spectrometry (UV-vis DRS) was used to

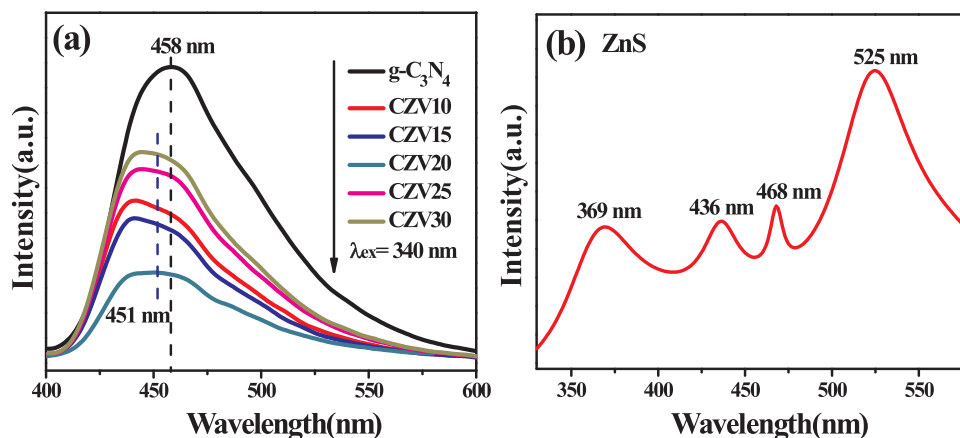


Fig. 6. PL spectra of as-synthesized (a) g-C₃N₄ and ZnS/g-C₃N₄ photocatalysts; (b) ZnS.

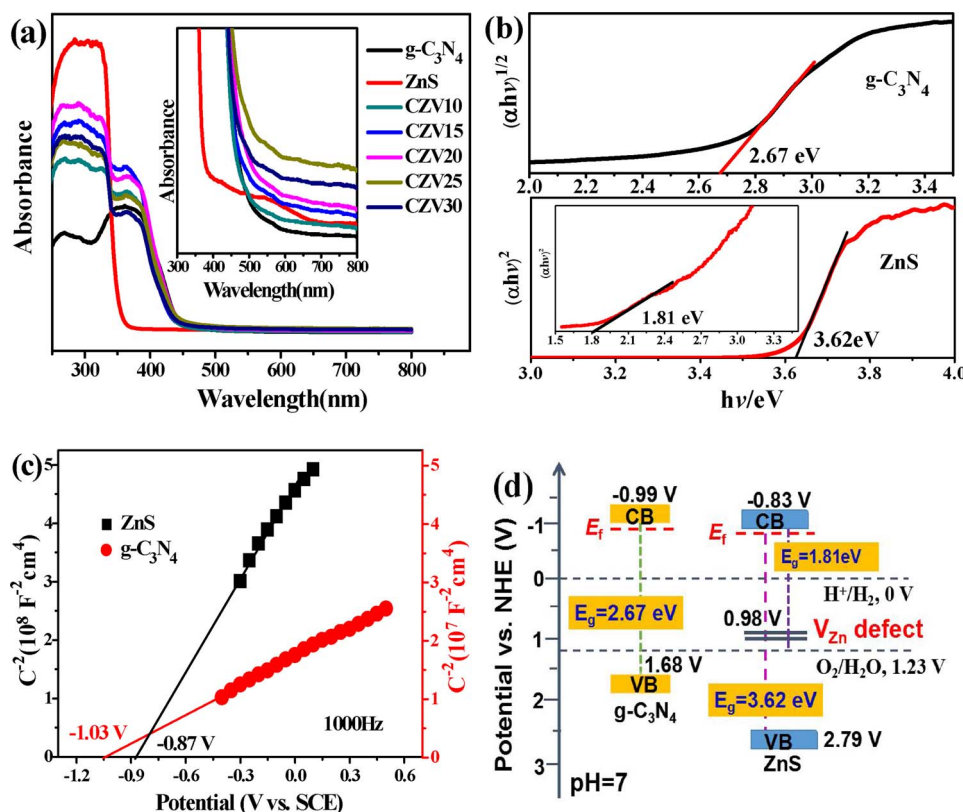


Fig. 7. (a) UV-vis DRS spectra of as-prepared pure g-C₃N₄, ZnS and ZnS/g-C₃N₄ samples; (b) The corresponding plots of $(\alpha h\nu)^2$ versus $h\nu$ of g-C₃N₄ and ZnS samples; Mott-Schottky plots of (c) g-C₃N₄ and (d) ZnS samples at frequency 1.0 kHz. (e) schematic illustration of band structures for g-C₃N₄ and ZnS.

investigate the effect of the zinc vacancies on the optical properties of ZnS/g-C₃N₄ heterojunction samples. As shown in Fig. 7a, the ZnS/g-C₃N₄ heterojunction samples show an enhanced light absorption with increasing of ZnS loading, which can be ascribed to the zinc vacancy of ZnS. In addition, the absorption spectrum of ZnS also has a strong photoabsorption edge around 681 nm in the visible-light region, which is related to its zinc vacancies. The corresponding band gap energies of pure g-C₃N₄ and ZnS samples are calculated by the transformed Kubelka-Munk function. As presented in Fig. 7b, the pristine g-C₃N₄ has a band gap value of 2.67 eV, while the ZnS has two band gap energies of 3.62 and 1.82 eV, which can be attributed to the main band gap and defect energy level created by zinc vacancy, respectively.

Mott – Schottky plots are employed to evaluate the flat-band potential (E_{fb}) of g-C₃N₄ and ZnS photocatalysts in 0.5M Na₂SO₄ electrolyte at frequencies 2.0, 1.5 and 1.0 kHz. As shown in Fig. 7c and Fig. S6, both g-C₃N₄ and ZnS exhibit the positive slopes of C^{-2} -E plots, indicating the n-type property of semiconductors [80]. The flat-band potential (E_{fb}) for g-C₃N₄ and ZnS are -1.03 and -0.87 V versus SCE, respectively. It is known that the conduction band potentials (E_{CB}) for n-type semiconductor is more negative about -0.1 or -0.2 V than its flat band potential [81]. And thus, the E_{CB} for g-C₃N₄ and ZnS are roughly reckon up to be -1.23 and -1.07 V versus SCE, that is, -0.99 and -0.83 V vs. normal hydrogen electrode (NHE) ($E_{\text{NHE}} = E_{\text{SCE}} + 0.241$ V). These positions thermodynamically enable the fast proton reduction for H₂ production. According to the band gap data in Fig. 7b, the valence band (VB) potentials of g-C₃N₄ and ZnS are 1.68 and 2.79 V versus NHE calculated by the equation: $E_{\text{VB}} = E_{\text{CB}} + E_{\text{g}}$. Furthermore, there is another E_{VB} for ZnS at about 0.98 V versus NHE. It should be noted that this E_{VB} for ZnS at about 0.98 V can be attributed to the zinc vacancies on ZnS created defect energy level within its band gap, which act as an acceptor levels for the charge carrier separation and enhance the visible-light photocatalytic response as well as improved charge carrier separation [65]. In

addition, this zinc vacancy defect energy level just in the middle of the ZnS bandgap, which is much well agreement with the two-photo absorption mechanism, and the two-step absorption via defect states has been reported to contribute near to the band edge of wide gap semiconductors [74–76]. So, the defect-assisted two-step absorption may be responsible to the visible-light photocatalytic activity of pure ZnS in this work. More clearly, the estimated positions of E_{CB} and E_{VB} for g-C₃N₄ and ZnS photocatalysts are illustrated in Fig. 7d. The band alignment between the g-C₃N₄ and ZnS suggests it is a typical Type II heterojunction structure [8,40]. This appropriate band-structure alignment between the g-C₃N₄ and ZnS create space charge accumulation/depletion at the interfaces that promotes the separation of photogenerated electrons and holes [8].

The interface charge transport behaviors of g-C₃N₄, ZnS and ZnS/g-C₃N₄ samples were studied by the Nyquist plots of electrochemical impedance spectroscopy (EIS) in dark. As shown in Fig. 8a, the radius of each arc is relevant to the resistance of the electrodes/electrolyte interface and the smaller radius corresponding with a lower charge-transfer resistance [51]. Apparently, the Zn deficient ZnS growth on g-C₃N₄ significantly decreased the charge-transfer resistance. And compared with those of samples, the CZV20 exhibits the smallest charge transfer resistance, suggesting that a faster interfacial charge transfer rate occurred in the ZnS/g-C₃N₄ heterojunctions.

To further explore the enhanced charge transfer and separation efficiency, the transient photocurrent-time curves ($I-t$ curves) of g-C₃N₄, ZnS and ZnS/g-C₃N₄ samples were measured by several on-off cycles of intermittent irradiation under visible light ($\lambda \geq 420$ nm). As displayed in Fig. 8b, it is clearly to observe that the CZV20 nanocomposite shows the highest photocurrent density compared with that of other samples, whereas the lowest photocurrent density is observed in the g-C₃N₄. This high photocurrent density further validate that CZV20 heterojunction display both the higher light utilization and more efficient electron transfer which caused by the Zn vacancies in the ZnS that enhanced

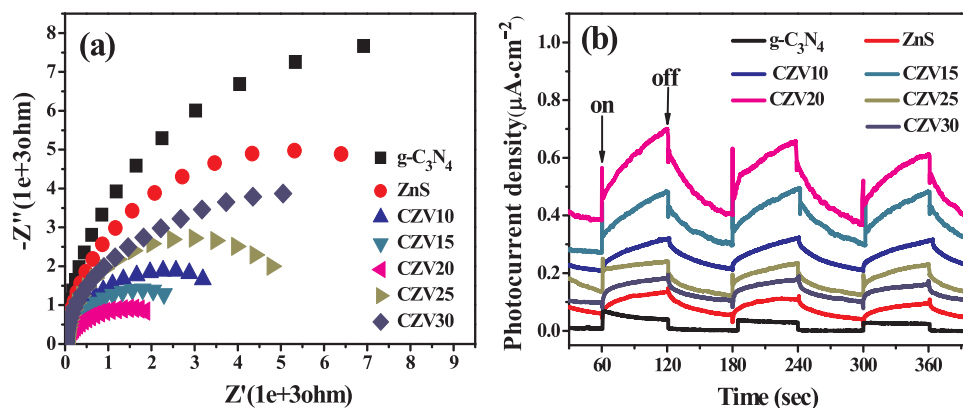


Fig. 8. (a) Nyquist plots of electrochemical impedance spectroscopy (EIS) for g-C₃N₄, ZnS, CZV10, CZV15, CZV20, CZV25 and CZV30 samples in 1.0 M KOH electrolyte; (b) Transient photocurrent response for g-C₃N₄, ZnS, CZV10, CZV15, CZV20, CZV25 and CZV30 samples in 0.5 M Na₂SO₄ electrolyte.

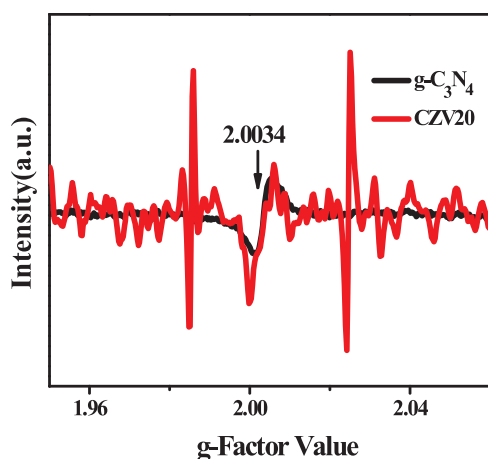


Fig. 9. EPR spectra of g-C₃N₄ and CZV20 samples.

visible-light absorption and charge separation. Additionally, the formed ZnS/g-C₃N₄ heterojunctions structure also beneficial to the interfacial charge transfer between the ZnS and g-C₃N₄.

Fig. 9 shows the electron paramagnetic resonance (EPR) spectra of the g-C₃N₄ and CZV20 samples. The EPR signal of g-C₃N₄ centering at $g = 2.0034$ can be assigned to an unpaired electron on the carbon atoms of the aromatic rings within π -bonded nanosize clusters [82]. An enhanced EPR signal was observed in the similar position for the spectrum of CZV20 heterojunction, indicating the much higher concentration of delocalized electrons. Consulting with the XPS results, the increase C/N ratio for CZV20 (1.43) compared with g-C₃N₄ (1.03) may

manifests the existence of nitrogen defects. These nitrogen defects generated in the hydrothermal treatment for g-C₃N₄ [26], which is very beneficial for the photogeneration of active radical pairs for catalytic reaction [66]. It is expected that these nitrogen defect sites have significant effect on the separation and transfer of charge carriers during photocatalytic hydrogen evolution process. It is reported that the nitrogen defects in g-C₃N₄ can enhance the visible light absorption by narrowing its band gap and suppress charge recombination, and thus improving the photocatalytic activity [24]. However, the light absorption edges of g-C₃N₄ and CZV20 samples are not changed, and the light absorption edge at 442 nm of all the samples of g-C₃N₄, CZV10 and CZV20 can clearly observed in Fig.S7. This results suggests that the amount of nitrogen defects in g-C₃N₄ is too little that not enough to red-shift the absorption edge, thus the nitrogen defect is also not the key factor for improving the photocatalytic activity compared with zinc vacancy.

3.2. Photocatalytic activity and stability

The photocatalytic H₂ evolution activities over various catalysts were evaluated under visible light irradiation ($\lambda \geq 420$ nm) with 0.35 M Na₂S and 0.25 M Na₂SO₃ aqueous solution as sacrificial agent. Zn vacancies is a crucial role for improving the photocatalytic H₂ evolution activity under visible light irradiation, which has been demonstrated in earlier experimental work [65]. The contents of ZnS were significantly influenced the photocatalytic H₂ evolution of ZnS/g-C₃N₄ composites, and the results are presented in Fig. 10a, all of the ZnS/g-C₃N₄ samples exhibit an enhanced photocatalytic H₂ production activity compared to pristine g-C₃N₄ and ZnS, achieving maximum for CZV20, and then decrease. The corresponding H₂ generation rates of g-

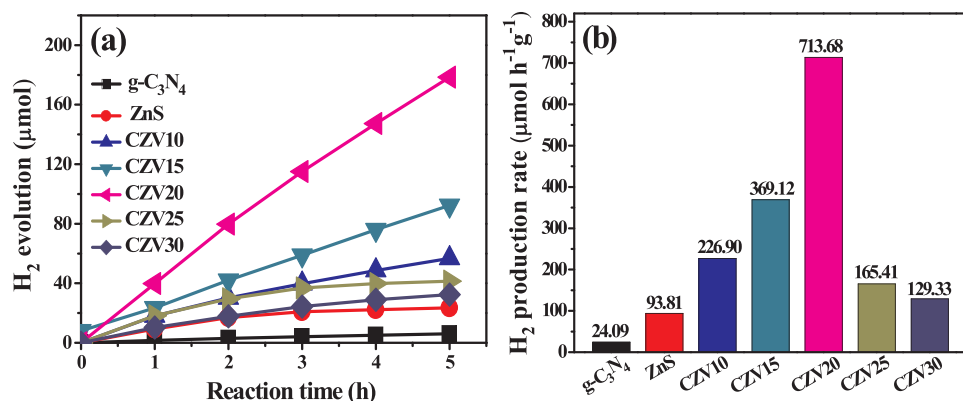


Fig. 10. (a) Time course of H₂ evolution and (b) the corresponding photocatalytic H₂ production rates of g-C₃N₄, ZnS and ZnS/g-C₃N₄ photocatalysts in 0.35 M Na₂S and 0.25 cM Na₂SO₃ aqueous solution under visible-light ($\lambda \geq 420$ nm) irradiation.

C₃N₄, ZnS and ZnS/g-C₃N₄ photocatalysts are presented in Fig. 10b, pure exhibits a rather low H₂ production rate of 24.09 $\mu\text{mol h}^{-1} \text{g}^{-1}$, arising from its limited visible-light absorption, poor charge transport capability and low specific surface area [24]. It is well known that ZnS is not has visible-light photocatalytic activity because its wide band gap (3.6 eV) [47]. Notably, in this work, the pure ZnS also exhibits a better H₂ production rate of 93.81 $\mu\text{mol h}^{-1} \text{g}^{-1}$ under visible light irradiation, which can be attributed to its enhanced visible-light absorption and excellent charge separation efficiency caused by the Zn vacancies in the ZnS sample. And the corresponding H₂ production rates are 226.90 $\mu\text{mol h}^{-1} \text{g}^{-1}$, 369.12 $\mu\text{mol h}^{-1} \text{g}^{-1}$, 713.68 $\mu\text{mol h}^{-1} \text{g}^{-1}$, 165.41 $\mu\text{mol h}^{-1} \text{g}^{-1}$ and 129.33 $\mu\text{mol h}^{-1} \text{g}^{-1}$ for the samples of CZV10, CZV15, CZV20, CZV25 and CZV30, respectively. The maximum rate of H₂ production was obtained over CZV20, which is about 30 times greater than that of the bare g-C₃N₄ (24.09 $\mu\text{mol h}^{-1} \text{g}^{-1}$). This superior photocatalytic H₂ evolution over ZnS/g-C₃N₄ can be ascribed to the enhanced visible-light absorption and excellent charge separation efficiency caused by the Zn vacancies in the ZnS [65]. Additionally, the formed ZnS/g-C₃N₄ heterojunctions structure is also beneficial to the interfacial charge transfer between the ZnS and g-C₃N₄, thus resulting in an obviously higher photocatalytic efficiency and H₂ evolution rate than that of obtained pure samples.

The stability tests of CZV20 nanocomposite are evaluated by the cycling H₂ evolution experiment, and the results are depicted in Fig. 11. It is clearly observed that the CZV20 nanocomposite photocatalyst do not have obvious decrease for H₂ generation in long-term photocatalytic reaction for four cycles usage. And the XRD characterization results (Fig. S8) also illustrate no structural change on the used sample after photocatalytic reaction. These results verify that ZnS/g-C₃N₄ nanocomposite photocatalysts possess excellent stability for photocatalytic H₂ production. The superior and stable photocatalytic H₂ evolution over CZV20 can be ascribed to the high charge separation efficiency and interfacial charge transfer caused by the Zn vacancies on ZnS and the formed ZnS/g-C₃N₄ heterojunctions structure, respectively.

3.3. Proposed photocatalytic mechanism for H₂ evolution

The photocatalytic hydrogen evolution reactions on the surface active sites are similar to those in electrolysis [43]. Thus, the electrochemical H₂ generation activities of g-C₃N₄, ZnS and ZnS/g-C₃N₄ electrodes were also investigated by the linear sweep voltammetry (LSV) method, as shown in Fig. S9. As expected, the ZnS/g-C₃N₄ samples display an enhanced cathodic current density with the Zn vacancy ZnS contents increasing at a similar potential range relative to g-C₃N₄ and ZnS, and the highest current density was observed for the CZV20 electrode, which clearly indicating the increased electron migration with optimized amount of Zn vacancies in ZnS/g-C₃N₄ nanocomposite interface. In addition, enlargement the polarization curve (*i* - *V*) of g-C₃N₄, ZnS and CZV20 samples in Fig. 12a, the CZV20 shows a lower

over-potential of ~ -0.43 V at the current density of $-50 \mu\text{A cm}^{-2}$ for hydrogen evolution reaction (HER), whereas the g-C₃N₄ and ZnS have a higher over-potential of ~ -0.69 V and ~ -0.65 V vs. SCE under the same current density, respectively. This low over-potential of CZV20 might be due to the fast electron transfer at ZnS/g-C₃N₄ interface to the active species (ZnS) surface to reduction the H₂O molecule. This results further confirmed that Zn vacancies ZnS has a significant effect on the HER activity of CZV20 heterostructure.

In order to understand the interactions between g-C₃N₄ and ZnS in the ZnS/g-C₃N₄ heterojunction during the HER kinetic process, the corresponding Tafel plots were constructed in the low current density region. Tafel slope *b* is determined by fitting polarization data to the Tafel Equation ($\eta = a + b \log |j|$, where η is the over-potential, *b* is the Tafel slope, and *j* is the current density) [80–83]. As depicted in Fig. 12b, a Tafel slope of ~ 66 mV dec⁻¹ for CZV20 is observed, which is great lower than that of the g-C₃N₄ (119 mV dec⁻¹) and ZnS (71 mV dec⁻¹). The low Tafel slope fall within the range of 40–120 mV dec⁻¹, suggesting that HER takes place via the Volmer – Heyrovsky mechanism (Volmer: $\text{H}_2\text{O} + \text{e}^- = \text{H}_{\text{ad}} + \text{OH}^-$, Heyrovsky: $\text{H}_{\text{ad}} + \text{H}_2\text{O} + \text{e}^- = \text{H}_2 + \text{OH}^-$) over the CZV20 electrodes surface [80–84]. This result indicates that the HER rate of CZV20 nanocomposite is faster than the g-C₃N₄ and ZnS. As a result, the high kinetic metrics including the low overpotential of ~ -0.45 V and smaller Tafel slope of ~ 66 mV dec⁻¹ demonstrate that the exceptional HER efficiency of the CZV20 nanocomposite.

On the basis of above results, a possible underlying photocatalytic hydrogen evolution mechanism is proposed in Scheme 1 for CZV20 heterojunction photocatalyst under visible-light irradiation. The much higher visible-light photocatalytic H₂ evolution activity of CZV20 is attributed to the both effective interface electrons transfer of its heterostructure and introduced zinc vacancies which created defect energy levels in the bandgap, thus improved charge carrier separation and enhanced the visible-light photocatalytic response. Under the visible light irradiation, the electrons and holes separate and accumulate in CB and VB of g-C₃N₄, respectively. The electrons further transfer to ZnS nanoparticles from the g-C₃N₄ due to the band-structure positions offset between the g-C₃N₄ and ZnS and then reduce H⁺ to molecule H₂, which not only can inhibit the recombination of photogenerated carriers, but also increase the reduction sites of H⁺ to H₂. Meanwhile, the holes are consumed by the electron donor, Na₂S and Na₂SO₃. Additionally, the ZnS also has the visible-light photocatalytic H₂ production activity though the two-photo excitation by the two-step absorption mechanism because the Zn vacancy defects narrow energy band gap. In two-photon excitation process, the initial photogenerated electrons jump to zinc vacancy defect energy level from VB of ZnS, and then this excited state electrons further photoexcited to the CB of ZnS by absorbing photons for H⁺ reduction. As a consequence, this V_{Zn} defect-assisted two-photo excitation mechanism over ZnS afford more photoexcited electrons for proton reduction. Thus, an enhanced visible-light photocatalytic activity for CZV20 heterojunction is obtained.

4. Conclusions

In conclusion, a novel ZnS/g-C₃N₄ photocatalyst has been prepared by decorating zinc vacancy ZnS on the surface of g-C₃N₄. The constructed ZnS/g-C₃N₄ heterojunction possess a low over-potential, extended absorption in the visible light region, and promoted photo-induced electron-holes separation capability. The intimate interfacial contact between g-C₃N₄ and ZnS nanoparticles accelerate the interfacial charge transfer and separation, as well as the existence zinc vacancies, improving the light-absorbing capacity and promoting photoinduced electron-holes separation capability of ZnS/g-C₃N₄ heterojunction. More attractively, the visible-light photocatalytic H₂ production activity for ZnS can be ascribed to the two-photo excitation by the two-step absorption mechanism because the existence Zn vacancy defects in the middle bandgap of ZnS. On the basis of these advantages, the V_{Zn}-rich

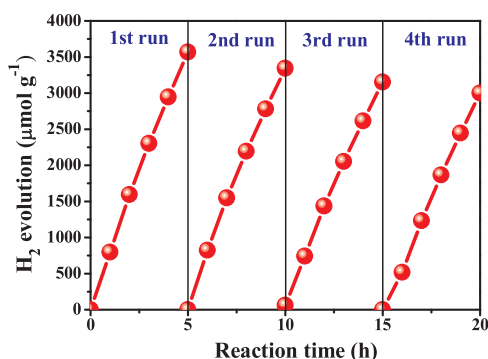


Fig. 11. Stability test of CZV20 for H₂ generation under visible light irradiation in 0.35 M Na₂S and 0.25 M Na₂SO₃ aqueous solution.

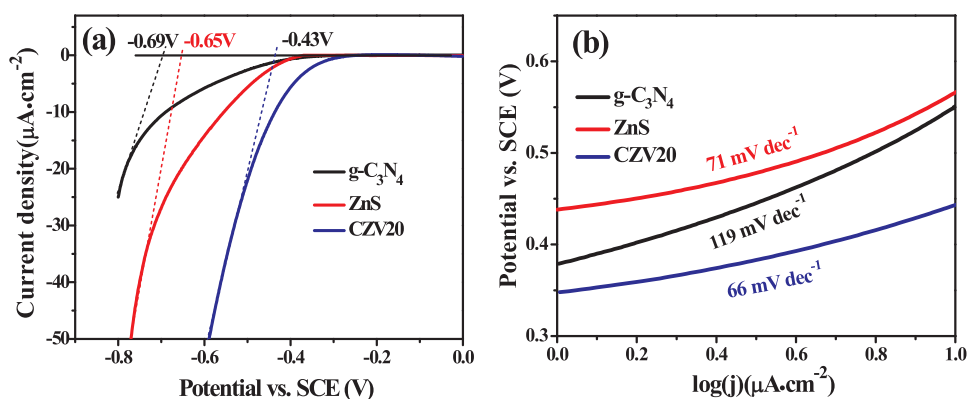
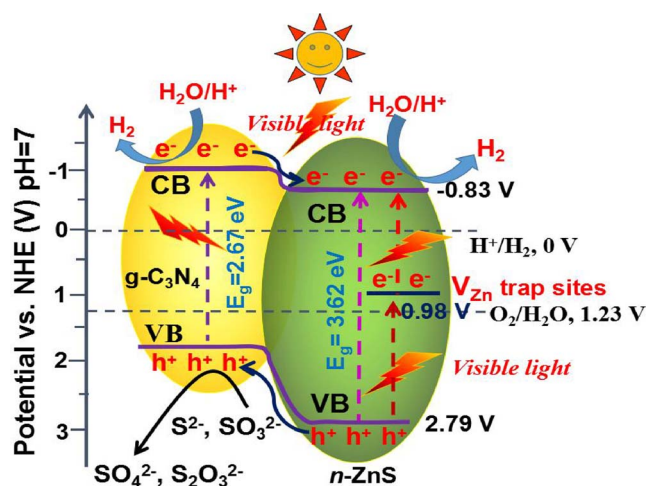


Fig. 12. (a) LSV curves and (b) Tafel slopes for g-C₃N₄, ZnS and CZV20 samples coated on ITO in 0.5 M Na₂SO₄ electrolyte. The scan rate was 5 mV s⁻¹.



Scheme 1. Photocatalytic mechanism for H₂ production over CZV20 heterojunction photocatalyst under visible-light irradiation.

CZV20 heterostructure exhibits the highest photocatalytic H₂ evolution rate (713.68 $\mu\text{mol h}^{-1} \text{g}^{-1}$) under visible light irradiation, which is about 30 and 7.6 times greater than that of g-C₃N₄ (24.09 $\mu\text{mol h}^{-1} \text{g}^{-1}$) and ZnS (93.81 $\mu\text{mol h}^{-1} \text{g}^{-1}$), respectively. The enhanced visible-light photocatalytic performance can be attributed to the synergistic effect of ZnS/g-C₃N₄ heterostructure and the two-photo absorption mechanism of zinc deficient-ZnS. This work presents a simple and highly effective strategy for developing high-efficiency g-C₃N₄-based photocatalytic materials with enhanced photocatalytic activity.

Acknowledgments

This work was financially supported by NSFC (21773113, 21273106). The authors would like to thank Analysis Center of Nanjing University for the sample characterization.

Appendix A. Supplementary data

Supplementary material related to this article can be found, in the online version, at doi: <https://doi.org/10.1016/j.apcatb.2018.02.006>.

References

- [1] X. Chen, S. Shen, L. Guo, S.S. Mao, Chem. Rev. 110 (2010) 6503–6570.
- [2] L. Yuan, C. Han, M.Q. Yang, Y.J. Xu, Int. Rev. Phys. Chem. 35 (2016) 1–36.
- [3] J.R. Ran, J. Zhang, J.G. Yu, M. Jaroniec, S.Z. Qiao, Chem. Soc. Rev. 43 (2014) 7787–7812.
- [4] J. Jin, C. Wang, X.N. Ren, S.Z. Huang, M. Wu, L.H. Chen, Nano Energy 38 (2017) 118–126.
- [5] S. Chen, T. Takata, K. Domen, Nat. Rev. Mater. 2 (2017) 17050.
- [6] S.Y. Tee, K.Y. Win, W.S. Teo, et al., Adv. Sci. 4 (2017) 1600337.
- [7] A. Kudo, Y. Miseki, Chem. Soc. Rev. 38 (2009) 253–278.
- [8] J.H. Zhang, M.W. Zhang, R.Q. Sun, X.C. Wang, Angew. Chem. 124 (2012) 10292–10296.
- [9] P. Ye, X.L. Liu, J. Iocozzia, Y.P. Yuan, L. Gu, G.S. Xu, Z.Q. Lin, J. Mater. Chem. A 5 (2017) 8493–8498.
- [10] X. She, J. Wu, J. Zhong, H. Xu, Y. Yang, R. Vajtai, et al., Nano Energy 27 (2016) 138–146.
- [11] K.L. Corp, C.W. Schlenker, J. Am. Chem. Soc. 139 (2017) 7904–7912.
- [12] J. Liu, H.Q. Wang, M. Antonietti, Chem. Soc. Rev. 45 (2016) 2308–2326.
- [13] S.W. Cao, J.X. Low, J.G. Yu, M. Jaroniec, Adv. Mater. 27 (2015) 2150–2176.
- [14] J. Liu, Y. Liu, N.Y. Liu, Y.Z. Han, X. Zhang, H. Huang, Y. Lifshitz, S.T. Lee, J. Zhong, Z.H. Kang, Science 347 (2015) 970–974.
- [15] Y. Zheng, L. Lin, B. Wang, X. Wang, Angew. Chem. Int. Ed. 54 (2015) 12868–12884.
- [16] Y.F. Guo, J. Li, Y.P. Yuan, L. Li, M.Y. Zhang, C.Y. Zhou, Z.Q. Lin, Angew. Chem. Int. Ed. 55 (2016) 14693–14697.
- [17] S. Ye, R. Wang, M.Z. Wu, Y.P. Yuan, Appl. Surf. Sci. 358 (2015) 15–27.
- [18] R. Wang, L. Gu, J.J. Zhou, X.L. Liu, F. Teng, C.H. Li, Y.H. Shen, Y.P. Yuan, Adv. Mater. Interfaces 2 (2015) 1500037.
- [19] Y.P. Yuan, L.S. Yin, S.W. Cao, L.N. Gu, G.S. Xu, P.W. Du, H. Chai, Y.S. Liao, C. Xue, Green Chem. 16 (2014) 4663–4668.
- [20] S.W. Cao, J.G. Yu, J. Phys. Chem. Lett. 5 (2014) 2101–2107.
- [21] M. Zhu, S. Kim, L. Mao, M. Fujitsuka, J. Zhang, X. Wang, T. Majima, Adv. Funct. Mater. 27 (2017) 1604328.
- [22] J.S. Zhang, Y. Chen, X.C. Wang, Energy Environ. Sci. 8 (2015) 3092–3108.
- [23] Y. Zheng, L.H. Lin, X.J. Ye, F.S. Guo, X.C. Wang, Angew. Chem. Int. Ed. 53 (2014) 11926–11930.
- [24] Z. Tong, D. Yang, Z. Li, Y. Nan, F. Ding, Y. Shen, Z. Jiang, ACS Nano 11 (2017) 1103–1112.
- [25] P. Niu, G. Liu, H.M. Cheng, J. Phys. Chem. C 116 (2012) 11013–11018.
- [26] Z. Hong, B. Shen, Y. Chen, B. Lin, B. Gao, J. Mater. Chem. A 1 (2013) 11754–11761.
- [27] P. Niu, L.C. Yin, Y.Q. Yang, G. Liu, H.M. Cheng, Adv. Mater. 26 (2014) 8046–8052.
- [28] H.J. Yu, R. Shi, Y.X. Zhao, T. Bian, Y.F. Zhao, C. Zhou, G.I.N. Waterhouse, Li. Zhu Wu, C. Ho Tung, T.R. Zhang, Adv. Mater. 29 (2017) 1605148.
- [29] Q.H. Liang, Z. Li, Z.H. Huang, F.Y. Kang, Q.H. Yang, Adv. Funct. Mater. 25 (2015) 6885–6892.
- [30] J. Zhang, X. Chen, K. Takanabe, K. Maeda, K. Domen, J.D. Epping, X. Fu, M. Antonietti, X. Wang, Angew. Chem. Int. Ed. 49 (2010) 441–444.
- [31] M.W. Zhang, X.C. Wang, Energy Environ. Sci. 7 (2014) 1902–1906.
- [32] H. Wang, B. Wang, Y. Bian, L.M. Dai, ACS Appl. Mater. Interfaces 9 (2017) 21730–21737.
- [33] G. Liu, P. Niu, C.H. Sun, S.C. Smith, Z.G. Chen, G. Qing (Max), Lu, H.M. Cheng, J. Am. Chem. Soc. 132 (2010) 11642–11648.
- [34] Z. An Lan, G.G. Zhang, X.C. Wang, Appl. Catal. B: Environ. 192 (2016) 116–125.
- [35] J. Wang, J. Cong, H. Xu, et al., ACS Sustain. Chem. Eng. 5 (2017) 5831–5841.
- [36] G.G. Zhang, Z. An Lan, L.H. Lin, S. Lin, X.C. Wang, Chem. Sci. 7 (2016) 3062–3066.
- [37] J.W. Fu, J.G. Yu, C.J. Jiang, B. Cheng, Adv. Energy Mater. (2017) 1701503.
- [38] S.W. Cao, J.X. Low, J.G. Yu, M. Jaroniec, Adv. Mater. 27 (2015) 2150–2176.
- [39] D.D. Zheng, G.G. Zhang, X.C. Wang, Appl. Catal. B: Environ. 179 (2015) 479–488.
- [40] J.Q. Yan, H. Wu, H. Chen, Y.X. Zhang, F.X. Zhang, S.F. Liu, Appl. Catal. B: Environ. 191 (2016) 130–137.
- [41] W.L. Gu, F.X. Lu, C. Wang, S. Kuga, L.Z. Wu, Y. Huang, M. Wu, ACS Appl. Mater. Interfaces 9 (2017) 28674–28684.
- [42] O. Elbanna, M. Fujitsuka, T. Majima, ACS Appl. Mater. Interfaces 9 (2017) 34844–34854.
- [43] J. Wen, J. Xie, H. Zhang, A. Zhang, Y. Liu, X. Chen, X. Li, ACS Appl. Mater. Interfaces 9 (2017) 14031–14042.
- [44] M. Zhu, S. Kim, L. Mao, M. Fujitsuka, J. Zhang, X. Wang, T. Majima, J. Am. Chem. Soc. 139 (2017) 13234–13242.
- [45] L. Ma, H. Fan, K. Fu, S. Lei, Q. Hu, ACS Sustain. Chem. Eng. 5 (2017) 7093–7103.
- [46] J. Xu, J. Gao, C. Wang, Y. Yang, L. Wang, Appl. Catal. B: Environ. 219 (2017) 101–108.
- [47] F. Shi, L. Chen, C. Xing, et al., RSC Adv. 4 (2014) 62223–62229.

- [48] P. Suyana, K.R. Sneha, B.N. Nair, et al., *RSC Adv.* 6 (2016) 17800–17809.
- [49] Z.X. Qin, F. Xue, Y.B. Chen, S.H. Shen, L.J. Guo, *Appl. Catal. B: Environ.* 217 (2017) 551–559.
- [50] L. Yao, D. Wei, Y. Ni, D. Yan, C. Hu, *Nano Energy* 26 (2016) 248–256.
- [51] M.K. Nowotny, L.R. Sheppard, A.T. Bak, J. Nowotny, *J. Phys. Chem. C* 112 (2008) 5275–5300.
- [52] D. Yan, Y. Li, J. Huo, R. Chen, L. Dai, S. Wang, *Adv. Mater.* (2017) 1606459.
- [53] X. Jiao, Z. Chen, X. Li, Y. Sun, S. Gao, W. Yan, et al., *J. Am. Chem. Soc.* 139 (2017) 7586–7594.
- [54] M. Kong, Y. Li, X. Chen, T. Tian, P. Fang, F. Zheng, X. Zhao, *J. Am. Chem. Soc.* 133 (2011) 16414–16417.
- [55] J. Wang, Z. Wang, B. Huang, et al., *ACS. Appl. Mater. Interfaces* 4 (2012) 4024–4030.
- [56] Y.H. Lv, W.Q. Yao, X.Q. Ma, C.S. Pan, R.L. Zong, Y.F. Zhu, *Catal. Sci. Technol.* 3 (2013) 3136–3146.
- [57] P. Wang, D. Wang, J. Lin, et al., *ACS Appl. Mater. Interfaces* 4 (2012) 2295–2302.
- [58] M.L. Guan, C. Xiao, J. Zhang, S.J. Fan, R. An, Q.M. Cheng, J.F. Xie, M. Zhou, B.J. Ye, Y. Xie, *J. Am. Chem. Soc.* 135 (2013) 10411–10417.
- [59] J. Li, H. Li, G. Zhan, L. Zhang, *Acc. Chem. Res.* 50 (2017) 112–121.
- [60] J. Li, X. Wu, W. Pan, G. Zhang, H. Chen, *Angew. Chem. Int. Ed.* 57 (2018) 491–495.
- [61] G. Wang, B. Huang, Z. Li, Z. Lou, Z. Wang, Y. Dai, M.H. Whangbo, *Sci. Rep.* (2015) 5.
- [62] Z. Fang, S. Weng, X. Ye, W. Feng, Z. Zheng, M. Lu, S. Lin, X. Fu, P. Liu, *ACS Appl. Mater. Interfaces* 7 (2015) 13915–13924.
- [63] F. Kurnia, H.N. Yun, R. Amal, N. Valanoor, J.N. Hart, *Sol. Energy Mater. Sol. Cells* 153 (2016) 179–185.
- [64] T. Mahvelati-Shamsabadi, E.K. Goharshadi, *Ultrason. Sonochem.* 34 (2017) 78–89.
- [65] X.Q. Hao, Y.C. Wang, J. Zhou, Z.W. Cui, Y. Wang, Z.G. Zou, *Appl. Catal. B: Environ.* 221 (2018) 302–311.
- [66] H.C. Lan, L.L. Li, X.Q. An, F. Liu, C.B. Chen, H.J. Liu, J.H. Qu, *Appl. Catal. B: Environ.* 204 (2017) 49–57.
- [67] C. Ma, H. Zhu, J. Zhou, Z. Cui, T. Liu, Y. Wang, Z. Zou, *Dalton Trans.* 46 (2017) 3877–3886.
- [68] T. Di, B. Zhu, B. Cheng, J. Yu, J. Xu, *J. Catal.* 352 (2017) 532–541.
- [69] L. Shao, D. Jiang, P. Xiao, L. Zhu, S. Meng, *Appl. Catal. B: Environ.* 198 (2016) 200–210.
- [70] D. Denzler, M. Olschewski, K. Sattler, *J. Appl. Phys.* 84 (1998) 2841–2845.
- [71] T. Mitsui, N. Yamamoto, T. Tadokoro, S. Ohta, *J. Appl. Phys.* 80 (1996) 6972–6979.
- [72] W. Zhang, X. Zeng, H. Liu, J. Lu, *J. Lumin.* 134 (2013) 498–503.
- [73] K. Manzoor, S.R. Vadera, N. Kumar, T. Kutty, *Mater. Chem. Phys.* 82 (2003) 718–725.
- [74] S.C. Pu, M.J. Yang, C.C. Hsu, et al., *Small* 2 (2006) 1308–1313.
- [75] R. Baltrameyunas, Y. Vaitkus, V. Gavryushin, *Sov. Phys. Solid State* 18 (1976) 1723–1725.
- [76] V.V. Borshch, P.E. Mozol, I.I. Patskun, et al., *Sov. Phys. Semicond.* 16 (1982) 213–214.
- [77] Y.H. Lu, W.H. Lin, C.Y. Yang, et al., *Nanoscale* 6 (2014) 8796–8803.
- [78] L. Ke, P.F. Li, X. Wu, S.J. Jiang, M.B. Luo, Y.H. Liu, Z.G. Le, C.H. Sun, S.Q. Song, *Appl. Catal. B: Environ.* 205 (2017) 319–326.
- [79] Z.F. Bian, T. Tachikawa, P. Zhang, M. Fujitsuka, T. Majima, *Nat. Commun.* 5 (2014) 3038.
- [80] W.L. Zhen, X.F. Ning, B.J. Yang, Y.Q. Wu, Z. Li, G.X. Lu, *Appl. Catal. B: Environ.* 221 (2018) 243–257.
- [81] S.S. Yi, J.M. Yan, B.R. Wulan, S.J. Li, K. Hua, L.Q. Jiang, *Appl. Catal. B: Environ.* 200 (2017) 477–483.
- [82] J. Zhang, G. Zhang, X. Wang, et al., *Angew. Chem.* 124 (2012) 3237–3241.
- [83] W.L. Zhen, H.B. Gao, B. Tian, J.T. Ma, G.X. Lu, *ACS Appl. Mater. Interfaces* 8 (2016) 10808–10819.
- [84] S.M. Kim, S.H. Jin, Y.J. Lee, M.H. Lee, *Electrochim. Acta* 252 (2017) 67–75.